CrossMark

JⁿM PAPERS

Elastohydrodynamics of contact in adherent sheets

Stéphane Poulain[1]**, Andreas Carlson**[1]**, Shreyas Mandre**[2] **and L. Mahadevan**[3,4,†]

[1]Mechanics Division, Department of Mathematics, University of Oslo, 0316 Oslo, Norway

[2]Mathematics Institute, University of Warwick, Coventry CV4 7AL, UK

[3]Paulson School of Engineering and Applied Sciences, Department of Physics, Harvard University, Cambridge, MA 02138, USA

[4]Department of Organismic and Evolutionary Biology, Harvard University, Cambridge, MA 02138, USA

Adhesive contact between a thin elastic sheet and a substrate arises in a range of biological, physical and technological applications. By considering the dynamics of this process that naturally couples fluid flow, long-wavelength elastic deformations and microscopic adhesion, we analyse a sixth-order thin-film equation for the short-time dynamics of the onset of adhesion and the long-time dynamics of a steadily propagating adhesion front. Numerical solutions corroborate scaling laws and asymptotic analyses for the characteristic waiting time for adhesive contact and for the speed of the adhesion front. A similarity analysis of the governing partial differential equation further allows us to determine the shape of a fluid-filled blister ahead of the adhesion front. Finally, our analysis reveals a near-singular behaviour at the moving elastohydrodynamic contact line with an effective boundary condition that might be useful in other related problems.

Key words: thin films, lubrication theory

1. Introduction

Adhesion of thin elastic films to substrates occurs in a range of problems in physical chemistry (Bell 1978), biology (Bongrand 1988; Dirks 2014; Butler *et al.* 2019), geophysics (Michaut 2011; Kavanagh, Engwell & Martin 2018) and engineering situations such as soft robotics (Salem *et al.* 2020) and wafer bonding (Bengtsson, Ljungberg & Vedde 1996; Tong & Gösele 1999; Han, Yu & Wang 2000; Pocius & Dillard 2002; Turner, Thouless & Spearing 2004; Rieutord, Bataillou & Moriceau 2005; Moriceau *et al.* 2011; Navarro *et al.* 2013; Radisson, Fournel & Charlaix 2015). Experimental and theoretical studies of adhesion focus on the microscale physical chemistry of bond formation (Bell 1978; Bell, Dembo & Bongrand 1984), on the mesoscale mechanics of elastic deformation of the

† Email address for correspondence: lmahadev@g.harvard.edu

film and on the squeeze flow in the gap (Cantat & Misbah 1999; Hosoi & Mahadevan 2004; Flitton & King 2004; Leong & Chiam 2010; Michaut 2011; Mani, Gopinath & Mahadevan 2012; Pihler-Puzović *et al.* 2012; Longley, Mahadevan & Chaudhury 2013; Lister, Peng & Neufeld 2013; Hewitt, Balmforth & De Bruyn 2015; Ball & Neufeld 2018; Juel, Pihler-Puzović & Heil 2018; Peng & Lister 2020; Wang & Detournay 2021), all of which are possibly affected by the presence of pre-wetted films, gravity or thermal fluctuations (Carlson 2018; Pedersen *et al.* 2019).

In the neighbourhood of the contact line between the elastic film and the substrate, the short-range adhesive interactions can lead to a high pressure that deforms the film and thence a squeeze flow, that in return affects the dynamics of adhesion. Theoretical models of soft adhesion usually focus only on the elastic and adhesive aspects of the process, typically neglecting the hydrodynamics (Springman & Bassani 2008, 2009; Rieutord, Rauer & Moriceau 2014). An early notable exception is the experimental and theoretical study of Rieutord *et al.* (2005) that used energetic arguments to determine the steady bonding speed of a silicon wafer as it comes into contact with a substrate, while also providing a scaling law for the local self-similar shape of the contact zone.

Here, we build on these previous works by completely characterizing the transient elastohydrodynamics of a soft adherent sheet. This problem has some similarities to the well studied problem of capillary interfaces seen in moving liquid–vapour contact lines and the dewetting of liquid films influenced by surface tension, which have a rich associated literature (de Gennes 1985; Eggers 2005; Bonn *et al.* 2009; Snoeijer & Eggers 2010; Snoeijer & Andreotti 2013). For example, in both the capillary and elastohydrodynamic cases, there is a near-singular behaviour at the contact line that is regularized by short-range effects which takes different forms: e.g. the presence of a pre-wetted layer between the elastic sheet and the substrate (Lister *et al.* 2013; Hewitt *et al.* 2015; Peng & Lister 2020), a vapour front (Hewitt *et al.* 2015; Ball & Neufeld 2018; Wang & Detournay 2018), elastic fracture (Lister, Skinner & Large 2019), etc. In the elastohydrodynamic case treated here, we model the microscale physics of adhesion using a van der Waals interaction potential driving the adhesion process between the elastic sheet and the substrate. As we will see, this allows us to characterize the multi-scale dynamics of the onset of adhesion, the steady motion of the moving contact zone and eventually to describe the dynamic shape of the propagating bulge ahead of the contact zone.

2. Mathematical model

2.1. *Thin-film elastohydrodynamics*

We begin with a description of the dynamics of a long and very wide elastic sheet of length ℓ, thickness $b \ll \ell$, separated from a solid substrate by a viscous thin film of density ρ, viscosity μ and thickness $h = h(x, t)$, where the sheet is initially flat with $h(x, t = 0) \equiv h_\infty$ and $h_\infty \ll \ell$ (figure 1a). The elastic sheet is attracted to a substrate by an intermolecular adhesion potential Φ defined between two flat surfaces and consisting of a van der Waals attraction and a strong short-range repulsion given by (Israelachvili 2011)

$$\Phi(h) = \frac{A}{6\pi} \left(\frac{1}{2h^2} - \frac{\sigma^6}{8h^8} \right), \tag{2.1}$$

with A the Hamaker constant, positive because we consider adhesion, and σ the equilibrium height at which the attractive and the repulsive parts of the resulting disjoining pressure balance each other. Evaluating the energy at this height yields the work of adhesion $W = \Phi(\sigma) = A/16\pi\sigma^2$. We note that altering the form of the Lennard-Jones
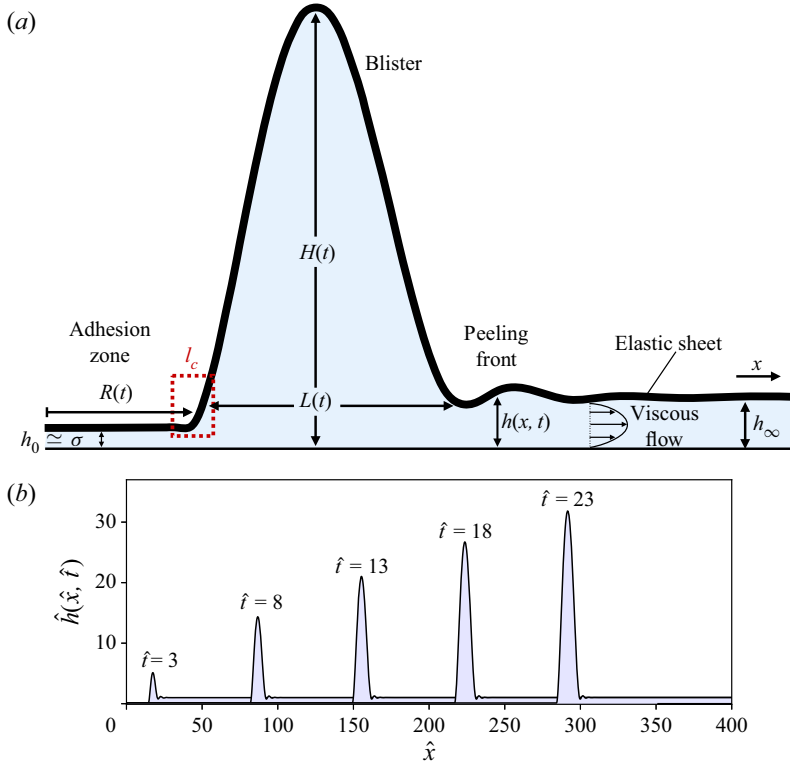
Figure 1. (*a*) Sketch showing the situation we study (not to scale): an elastic sheet is separated from a solid substrate by a thin viscous film of height $h = h(x, t)$, initially with uniform height h_∞. The disjoining pressure $-\Phi_h$, originating from an intermolecular interaction potential, brings the sheet towards the substrate at an equilibrium distance h_0 close to σ (left). This leads to the formation of an adhesion front of length $R(t)$ that grows in time. The fluid-filled blister ahead of the adhesion front moves with a constant speed $c = dR/dt$. As the adhesion front grows it displaces the viscous fluid into the blister, making its horizontal extent $L(t)$ and height $H(t)$ grow in time. The dotted rectangle denotes the adhesion front, the small inner region where viscous, elastic and adhesive forces are all comparable in magnitude. (*b*) Results from a numerical simulation of (2.5) with $\hat\sigma = 0.12$ at different times. The sheet is brought into contact with the substrate first at $\hat{x} = 0$ because of the initial profile $\hat{h}(\hat{x}, \hat{t} = 0) = 1 - 0.1(1 - \tanh^2(\hat{x}/5))$ that induces a perturbation. After a short transient phase associated with the formation of a contact zone characterized by the waiting time $\hat{T}$, see § 3.1 and (3.1), the adhesion front propagates in time, displacing the fluid into a growing and translating blister.

potential in (2.1) does not change the physical picture as long as the balance leads to a stable static equilibrium, and is discussed further in § 4.2.

The adhesive interactions cause the elastic sheet to deform; the balance of transverse forces for long-wavelength deformations of the sheet yields the equation (Landau & Lifshitz 1986)

$$p = Bh_{xxxx} - \Phi_h, \tag{2.2}$$

where $(\cdot)_x \equiv \partial(\cdot)/\partial x$. Here, p is the local pressure along the sheet, $-\Phi_h$ is the disjoining pressure and Bh_{xxxx} is the contribution from elasticity for a plate with a bending stiffness $B = Eb^3/12(1 - \nu^2)$ (with E its Young's modulus and ν its Poisson's ratio). Equation (2.2) is only valid under the assumptions that slopes are small, i.e. $h_x^2 \ll 1$, and that the deformations of the sheet remain comparable to its thickness, allowing us to neglect geometrical nonlinearities in the shape of the sheet. We further note that we have also

neglected stretching effects that are expected to be negligible for cylindrical deformations of elastic sheets that are unconstrained and free at one end; experimental results in elastohydrodynamics with unconstrained sheets show that the theory neglecting stretching is reasonable (Berhanu *et al.* 2019; Pedersen *et al.* 2019).

When the sheet evolves in response to the attractive adhesive interaction which brings it in proximity to the substrate, the interstitial fluid is squeezed out. If the aspect ratio of the gap is small, i.e. $\epsilon = h_\infty/\ell \ll 1$, and the Reynolds number of the flow based on the speed of the adhesion front c (discussed next in § 3.2) is small, i.e. $Re = \epsilon \rho h_\infty c/\mu \ll 1$, then the flow in the interstitial gap can be described via lubrication theory and yields the equation (Batchelor 1967; Oron, Davis & Bankoff 1997) $h_t - (h^3 p_x/12\mu)_x = 0$, which, using (2.2), reads

$$h_t - \left(\frac{h^3}{12\mu} \left(B h_{xxxx} + \frac{A}{6\pi} \left(\frac{1}{h^3} - \frac{\sigma^6}{h^9} \right) \right)_x \right)_x = 0, \qquad (2.3)$$

where we have assumed the no-slip boundary condition for the fluid along the two solid surfaces.

2.2. *Scaling and boundary conditions*

To scale the variables and reduce the parameters in the system we define the following quantities:

$$\hat{h} = \frac{h}{h_\infty}, \quad \hat{x} = \frac{x}{x_\infty}, \quad x_\infty = h_\infty \left(\frac{6\pi B}{A} \right)^{1/4}, \quad \hat{t} = \frac{t}{\tau_\mu}, \quad \tau_\mu = \frac{12\mu h_\infty^3 B^{1/2}}{(A/6\pi)^{3/2}}.$$
$$(2.4a\text{--}e)$$

Here, the length scale x_∞ arises from the balance between the attractive part of the disjoining pressure and the bending pressure at the far-field height h_∞. Then the problem is characterized by the single dimensionless number $\hat{\sigma} \equiv \sigma/h_\infty$, the ratio between the equilibrium height σ and the far-field height h_∞, and (2.3) can be rewritten as

$$\hat{h}_{\hat{t}} - \left(\hat{h}^3 \left(\hat{h}_{\hat{x}\hat{x}\hat{x}\hat{x}} + \left(\frac{1}{\hat{h}^3} - \frac{\hat{\sigma}^6}{\hat{h}^9} \right) \right)_{\hat{x}} \right)_{\hat{x}} = 0. \qquad (2.5)$$

In the rest of the paper, we will present results in the text in both dimensional and scaled form, but all figures will be based solely on scaled quantities. While the characteristic longitudinal scale is expected to be x_∞, near the effective contact line, i.e. the zone where the sheet deforms substantially from its flat state owing to fluid pressure, we expect the adhesive equilibrium height σ to be relevant. As we will see later, this leads to another natural lateral scale $l_c = \hat{\sigma} x_\infty = \sigma (6\pi B/A)^{1/4}$, so that the extent of the adhesion front scales as $\sigma(B/A)^{1/4}$. As $\hat{\sigma} \to 0$, the zone becomes very narrow with an accompanying singular behaviour in the dynamics of the contact line. We note, however, that the slope of the sheet at the apparent contact line scales as $h_x \sim \sigma/l_c \sim (A/B)^{1/4} \ll 1$, and is thus consistent with the long-wavelength approximation used to derive the governing equation (2.3) and (2.5).

In order to complete the problem associated with (2.5), we need to prescribe a total of six boundary conditions. We assume symmetry at the centre of the sheet $\hat{x} = 0$,

so that

$$\hat{h}_{\hat{x}}(\hat{x} = 0, \hat{t}) = \hat{h}_{\hat{x}\hat{x}\hat{x}}(\hat{x} = 0, \hat{t}) = \hat{p}_{\hat{x}}(\hat{x} = 0, \hat{t}) = 0, \qquad (2.6)$$

and that the right (and left) ends of the sheet are flat and consistent with the initial conditions, so that as $\hat{x} \to \infty$

$$\hat{h}_{\hat{x}}(\hat{x} \to \infty, \hat{t}) = \hat{h}_{\hat{x}}(\hat{x} \to \infty, \hat{t} = 0), \quad \hat{h}_{\hat{x}\hat{x}}(\hat{x} \to \infty, \hat{t}) = \hat{h}_{\hat{x}\hat{x}}(\hat{x} \to \infty, \hat{t} = 0), \quad (2.7a)$$

$$\hat{p}(\hat{x} \to \infty, \hat{t}) = \hat{\Phi}_{\hat{h}}(\hat{h}(\hat{x} \to \infty, \hat{t} = 0)). \qquad (2.7b)$$

The mathematical model (2.5)–(2.7) provides a compact formulation of the elastohydrodynamics coupling the microscopic physics of adhesion to elastic film deformations and interstitial fluid flow.

2.3. *Numerical implementation*

To characterize the adhesion dynamics we solve numerically (2.5) with boundary conditions (2.6) and (2.7). We use a finite element method with linear elements for $\hat{h}$, $\hat{h}_{\hat{x}\hat{x}}$ and $\hat{h}_{\hat{x}\hat{x}\hat{x}\hat{x}}$ coupled with a first-order and implicit time integration scheme. The domain size (sheet length) is made large enough so that it does not affect the numerical results, i.e. we ensure that the boundary of the domain remains far enough away from the peeling front, at least 100 dimensionless units, so as to not affect its dynamics. The adhesion front is well resolved with $\Delta\hat{x} \lesssim \hat{l}_c/50$ there, and we use an adaptive mesh refinement method to limit the number of degrees of freedom in the other regions. We mainly focus on an initially flat sheet, starting with an initial condition $\hat{h}(\hat{x}, \hat{t} = 0) = 1 - 0.1(1 - \tanh(\hat{x}/\beta)^2)$ in order to induce a perturbation as a small dip that triggers adhesion at $\hat{x} = 0$. We verified that the results of the simulations are independent of the size of the perturbation β once adhesion has been triggered, and unless otherwise noted we used $\beta = 2$. We also considered two additional initial and far-field profiles, a linear one and a quadratic one, which we discuss further in § 4.3.

3. Analysis

In figure 1(*b*) we show that, following the onset of adhesion at short times, a fluid-filled blister forms and then propagates steadily as the adhesive front $R(t)$ moves and the blister grows simultaneously. We now turn to discuss these different phenomena in turn.

3.1. *Waiting time estimate*

When the disjoining pressure $-\Phi_h$ brings the sheet closer to the substrate non-uniformly, the resulting pressure gradients cause fluid to be squeezed longitudinally, bringing the sheet even closer to the substrate until it locally reaches a height consistent with the equilibrium height σ. We define this as the time for the onset of adhesive contact τ_w. Carlson & Mahadevan (2016) showed that if there were no repulsive part to the intermolecular potential, i.e. in the limit $\hat{\sigma} \to 0$, the flat state is linearly unstable to long-wavelength perturbations, and further that contact would occur as a finite-time singularity with $h(x = 0, t) \sim h_\infty(1 - t/\tau_w)^{1/3}$, with $\tau_w \sim \tau_\mu$ the viscous time scale defined in (2.4*a*–*e*). In the present situation, a linear stability analysis of (2.5) with a perturbation $\hat{h}(\hat{x}, \hat{t}) = 1 + \hat{\varepsilon} \exp(i\hat{k}\hat{x} + \hat{\omega}\hat{t})$, $|\hat{\varepsilon}| \ll 1$, yields the dispersion relation $\hat{\omega} = -\hat{k}^2(\hat{k}^4 - 3 + 9\hat{\sigma}^6)$, and we expect the repulsive part of the disjoining pressure to
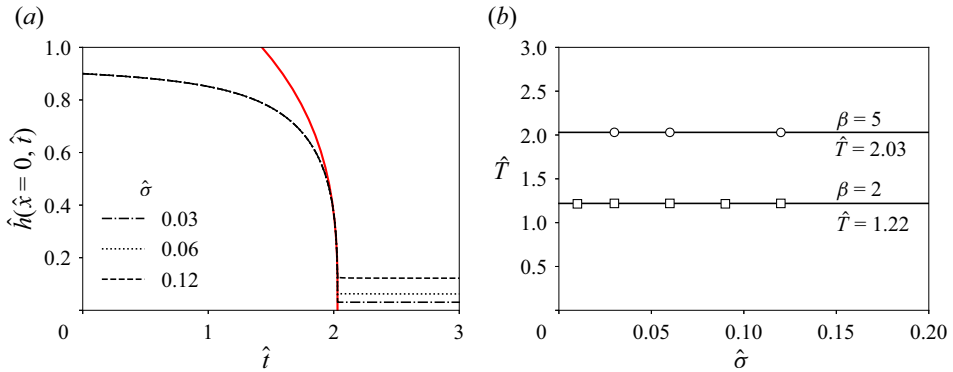
Figure 2. (a) Evolution of the height of the elastic sheet at $\hat{x} = 0$ obtained by solving (2.5) with an initial perturbation $\hat{h}(\hat{x}, \hat{t} = 0) = 1 - 0.1(1 - \tanh(\hat{x}/\beta)^2)$, with $\beta = 5$, and for three values of $\hat{\sigma}$. For $\hat{t} < \hat{T} = 2.03$ the different curves cannot be distinguished. The solid line represents the scaling $\hat{h}(\hat{x} = 0, \hat{t}) \sim (1 - \hat{t}/\hat{T})^{1/3}$ expected for $\hat{\sigma} \ll 1$, with a fitted prefactor. (b) Waiting time for onset of adhesion for two values of the size β of the initial perturbation. The markers represent numerical simulations (squares: $\beta = 2$; circles: $\beta = 5$), and the solid lines represent constant values of $\hat{T}$. We extract the waiting time from the numerical simulations by defining it as the time it takes for $\hat{h}(\hat{x} = 0, \hat{t})$ to go from the initial condition down to $1.1\hat{\sigma}$.

only play a role very close to the substrate, with the adhesion time following the scaling law $\tau_w \sim \tau_\mu$ independently of $\hat{\sigma}$:

$$\tau_w = \hat{T}\frac{12\mu h_\infty^3 B^{1/2}}{(A/6\pi)^{3/2}}, \tag{3.1}$$

where the dimensionless adhesion time $\hat{T}$ is a constant. In figure 2, we show that our numerical simulations follow this scaling relation. While the value of $\hat{T}$ depends on the initial perturbation to the flat sheet, for $\hat{t} \gg \hat{T}$, the evolution of the system is independent of initial conditions. It may be useful to compare (3.1) with the capillary time for the rupture of a thin liquid film. In this situation, the rupture time scales as $\mu h_\infty^5 \gamma_{LV}/A^2$ (Zhang & Lister 1999; Carlson et al. 2013), where γ_{LV} is the liquid–vapour surface tension, and shows a stronger dependence on both the Hamaker constant A and the far-field height h_∞, reflecting the intuition that elastohydrodynamic touchdown is slowed down by the effectively larger 'stiffness' (at short length scales) of an elastic sheet relative to a capillary interface.

3.2. Scale and speed of the adhesion front

After first contact, once $h(x = 0, t) \simeq \sigma$, the adhesion front grows longitudinally and a localized fluid-filled blister starts to move rightwards (a symmetric one grows leftwards as well). Defining the apparent contact line as the point of maximum curvature, i.e. $R(t) = \arg\max_x(h_{xx}(x, t))$, in figure 3(a) we show our numerical simulations that are consistent with $R(t)$ moving at a constant speed $c = dR/dt$. To characterize the speed of the contact line, we first consider the integrated viscous dissipation rate. In figure 3(b), we show that the viscous power per unit width $\int_0^{+\infty} \int_0^h \mu u_y^2 \, dy \, dx = \int_0^{+\infty} h^3(x, t)p_x^2(x, t) \, dx/12\mu$ becomes time independent at long times, where $u(x, y)$ is the Poiseuille velocity profile (Batchelor 1967; Oron et al. 1997) used to derive (2.3). At a scaling level, the viscous dissipation scales as $\mu(c/\sigma)^2 \Omega$, where $\Omega \sim \sigma l_c$. Balancing the driving adhesive power
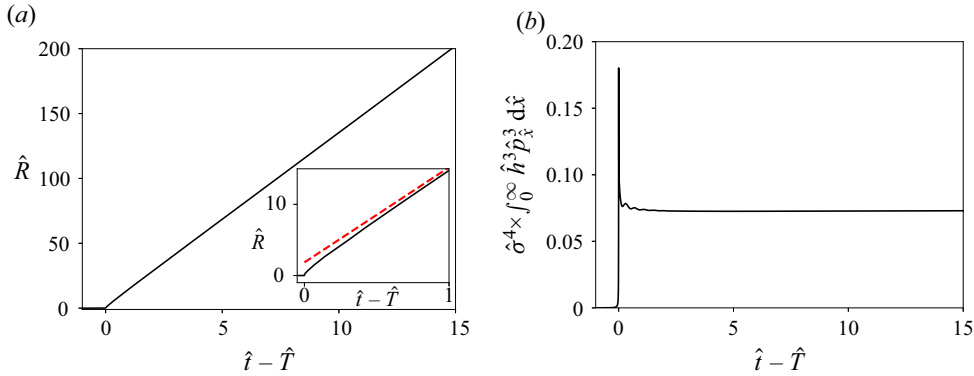
947 A16-6

Figure 3. Data from a numerical simulation of (2.5) with $\hat{\sigma} = 0.12$. (a) Growth of the adhesion front $\hat{R}(\hat{t})$. For $\hat{t} > \hat{T}$, $\hat{R}(\hat{t})$ becomes linear. The inset shows the behaviour for $\hat{t} \approx \hat{T}$, highlighting the fact that the constant speed (dashed line) is quickly reached. (b) The instantaneous viscous dissipation power, $\int_0^{+\infty} \hat{h}^3(\hat{x}, \hat{t}) \hat{p}_{\hat{x}}^2(\hat{x}, \hat{t}) \, \mathrm{d}\hat{x}$, shows a sharp increase at the onset of adhesion and then evolves towards a constant value.

per unit width cA/σ^2 with the viscous power $\mu c^2 l_c / \sigma$ then yields $c \sim A^{5/4}/\mu\sigma^2 B^{1/4}$. We note that this last scaling is the same as the one given by Rieutord *et al.* (2005) and Navarro *et al.* (2013), but with σ replaced by a molecular mean free path used as an arbitrary cutoff length, unlike in our case, where it is the equilibrium height arising naturally from the intermolecular potential Φ. Following the brief discussion in § 2.2, if we use the relevant height scale in the adhesion front σ and the relevant length scale l_c, this leads to the following dimensionless quantities:

$$\tilde{h} = \frac{h}{\sigma}, \quad \tilde{\eta} = \frac{\eta}{l_c}, \quad l_c = \sigma \left(\frac{B}{A/6\pi} \right)^{1/4}, \quad \tilde{t} = \frac{t}{\hat{\sigma}^3 \tau_\mu}, \quad (3.2a\text{--}d)$$

it follows that the speed of the adhesion front is

$$c = \tilde{C} \frac{(A/6\pi)^{5/4}}{12\mu\sigma^2 B^{1/4}}, \quad \hat{c} = \tilde{C}\hat{\sigma}^{-2}, \quad (3.3a,b)$$

where the dimensionless constant $\tilde{C}$ is yet to be determined.

Figure 4(a) shows that our simulations indeed follow (3.3a,b). To go beyond this scaling analysis and predict the value of the constant $\tilde{C}$, we look for a travelling wave solution as in related problems (Lister *et al.* 2013; Wang & Detournay 2021). Letting $h(x, t) = f(\eta)$ with $\eta = x - ct$ transforms the governing partial differential equation (2.3) into an ordinary differential equation, which we make dimensionless (3.2a–d) and integrate once by introducing the constant $h_0 = \sigma\tilde{h}_0$ such that $h \to h_0$ as $\eta \to -\infty$. We note that h_0 is not necessarily equal to σ, even though we expect the two values to be close, since the pressure gradient vanishes for any constant height profile. This leads to the nonlinear ordinary differential equation

$$\tilde{C}(\tilde{f} - \tilde{h}_0) + \tilde{f}^3 \left(\tilde{f}'''' + \frac{1}{\tilde{f}^3} - \frac{1}{\tilde{f}^9} \right)' = 0, \quad (3.4)$$

with $(.)' = \mathrm{d}(.)/\mathrm{d}\tilde{\eta}$. This fifth-order nonlinear ordinary differential equation with two unknown parameters, $\tilde{h}_0$ and $\tilde{C}$, is subject to a pair of constraints. The first is that as
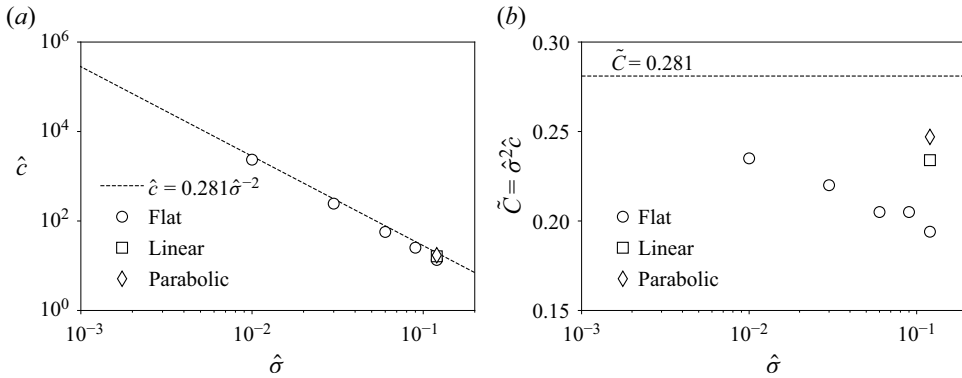
Figure 4. (*a*) Speed $\hat{c}$ of the adhesion front for different initial conditions and far-field profiles (discussed in § 4.3), with $\hat{\sigma} = 0.12, 0.09, 0.06, 0.03, 0.01$ and obtained by solving (2.5). The dashed line represents (3.3*a*,*b*), with the prefactor 0.281 obtained by solving (3.4). (*b*) Same data normalized according to (3.2*a–d*), highlighting the better agreement between numerical simulations and theory as $\hat{\sigma}$ decreases.

$\tilde{\eta} \to -\infty, \tilde{f} \to \tilde{h}_0$. The second is that, when $\tilde{\eta} \to +\infty$, (3.4) simplifies to $\tilde{C}\tilde{f} + \tilde{f}^3\tilde{f}'''' = 0$ and we expect a self-similar solution of the form $\tilde{f}(\tilde{\eta}) \sim (243/280)^{1/3}\tilde{C}^{1/3}\tilde{\eta}^{5/3}$.

Using these conditions, we solve numerically (3.4) using the bvp4c routine implemented in MATLAB (see Appendix A for details) and find that $\tilde{C} = 0.281$, $\tilde{h}_0 = 1.017$. The maximum curvature of the profile is $\tilde{\kappa}_{max} = 0.551$ and is discussed further in § 6. Figure 4 shows that the value of $\tilde{C}$ is qualitatively consistent with our simulations; although there are deviations of up to 40 %. This disagreement likely comes from the finite ratio between the size of the adhesion front and the domain size leading to a lack of scale separation; indeed, as $\hat{\sigma}$ becomes smaller, we see a tendency towards the asymptotic state consistent with the self-similar dynamics. In figure 5(*a,b*), we show the comparison of the height profile from the numerical simulation of the reduced equation (3.4) and the profile obtained from the full partial differential equation (2.5) with $\hat{\sigma} = 0.12$. While the overall agreement is good, it may seem surprising that h_0 differs from σ, even if by only 2 %. To understand this, we note that the dispersion relation discussed in § 3.1 shows that a profile with constant height h_0 is linearly stable if $h_0/\sigma < 3^{1/6} \simeq 1.20$. As a point of comparison with the much better studied case of dewetting of liquid films, we note that there too the height ahead of the moving contact line differs slightly from the equilibrium height (Eggers 2005).

3.3. *Shape, size and dynamics of fluid-filled blister*

Having determined the waiting time τ_w, the speed c of the apparent contact line and the shape of the adhesion front, we now turn to a description of the blister developing ahead of the adhesion front. We characterize the blister in terms of its maximum height $H(t)$ and width $L(t)$. We expect that once the blister has grown sufficiently with $H(t) \gg h_\infty$, its shape becomes independent of the local adhesion, even as it slowly spreads while gathering fluid. To describe the shape of the blister, we adapt the analysis of related problems by Peng *et al.* (2015) and Wang & Detournay (2021). In a moving frame with $\eta = x - ct$, the height profile of the blister $h_b(\eta)$ can be obtained by integrating (2.2) and considering a spatially invariant pressure profile $p \simeq Bh_{\eta\eta\eta\eta}$, neglecting the van der Waals interaction. Using clamped boundary conditions, i.e. $h = 0$, $h_\eta = 0$ at the apparent contact line defined
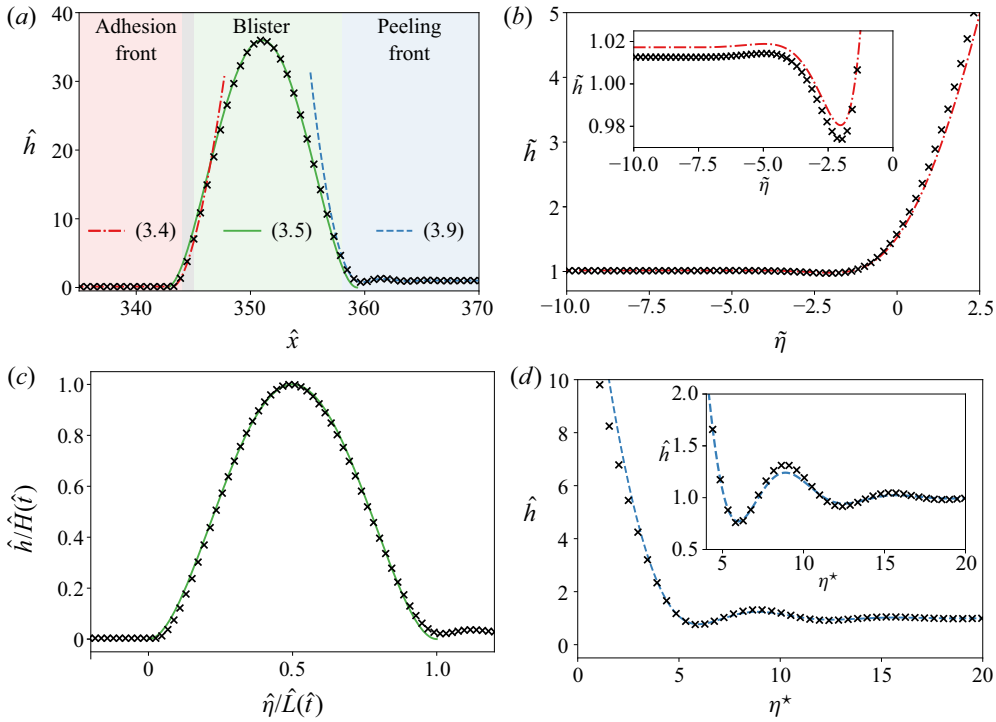
Figure 5. (*a*) Comparisons of the height profile between the asymptotic results (lines) and a numerical simulation of (2.5) with $\hat{\sigma} = 0.12$ at time $\hat{t} - \hat{T} = 27.34$ (crosses). Markers are spaced to facilitate readability and do not correspond to the numerical grid. Other panels show details of each region in a travelling reference frame η, rescaled differently in each region according to the non-dimensionalizations discussed in the text. (*b*) Adhesion region. The line is the numerical solution of (3.4). (*c*) Blister. The line is (3.5), where $\hat{H}$ and $\hat{L}$ have been extracted from the numerical profile. (*d*) Peeling front. The line is the numerical solution of (3.9).

as $\eta = 0$ and at the peeling front $\eta = L(t)$ then gives

$$h_b(\eta, t) = 16 \frac{H(t)}{L^4(t)} \eta^2 (L(t) - \eta)^2. \tag{3.5}$$

To determine the height $H(t)$ and width $L(t)$ of the blister we impose fluid mass conservation and a shape continuity condition at the peeling front. Assuming that most of the displaced fluid accumulates in the blister and that the volume of the remaining fluid between the sheet and the substrate after adhesion is negligible, i.e. $\sigma/h_0 \simeq \hat{\sigma} \ll 1$, we can write

$$\int_0^{L(t)} h_b(\eta, t) \, d\eta = \int_0^{ct} h(x, 0) \, dx. \tag{3.6}$$

For an initially flat sheet, $\int_0^{ct} h(x, 0) dx = cth_\infty$. Then using (3.5), we find that (3.6) simplifies to $16H(t)L(t)/30 = cth_\infty$.

At $\eta = L(t)$, the solution within the blister must be consistent with the dynamics of the peeling front that is observed numerically in figure 5(*a,d*). We assume that the speed c of the adhesion (healing) front is the same as that of the peeling front, i.e. that the blister moves much faster than its lateral growth rate dL/dt. At the peeling front, the far-field height h_∞ and the peeling length $L_p = (Bh_\infty^3/12\mu c)^{1/5}$ conspire to yield a local curvature
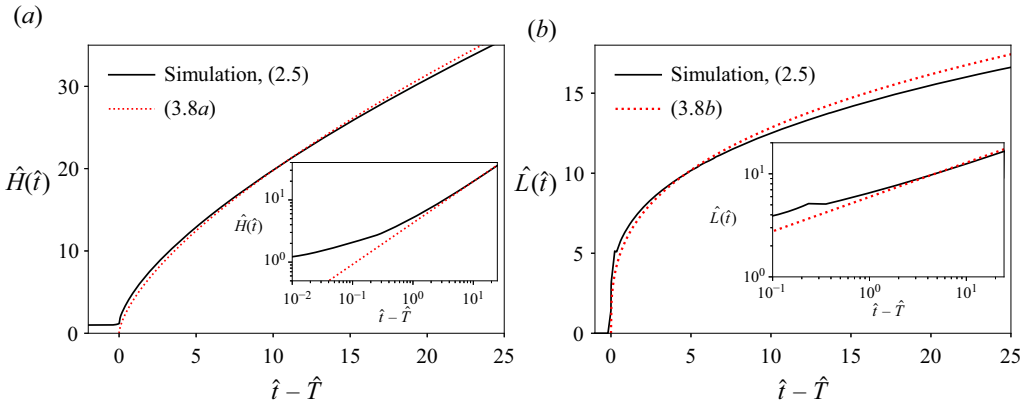
947 A16-9

Figure 6. Characterization of the blister with $\hat{\sigma} = 0.12$, showing the time evolution of (a) its maximal height $\hat{H}$ and (b) its lateral extent $\hat{L}$. Solid lines represent numerical solutions of (2.5) and dotted lines are the predictions (3.8). Numerically, we define $\hat{H}$ as the maximal height of the sheet and $\hat{L}$ as the distance between the two local minima of $\hat{h}$ surrounding the point of maximal height. The time is shifted by the adhesion time because the analysis of the blister is only relevant once a blister is actually formed.

that scales as $\kappa \sim h_\infty/L_p^2$, which then gives (up to a prefactor)

$$c = \frac{Bh_\infty^{\frac{1}{2}}}{12\mu} \left(\frac{\kappa}{1.35}\right)^{5/2}. \tag{3.7}$$

Here, the prefactor 1.35 comes from the matching procedure between the blister and the peeling front first carried out by Lister *et al.* (2013), and which we briefly discuss next in §3.4.

Since the adhesion speed is determined by the behaviour in the adhesion zone outside of the blister, and is given by (3.3a,b), we interpret (3.7) as an expression that determines the curvature as a function of the speed. Using the blister profile (3.5) yields the curvature at the peeling front $\kappa = h_{b\eta\eta}(\eta = L(t)) = 32H(t)/L^2(t)$. Substituting this value in (3.7) gives a second relation between $H(t)$ and $L(t)$. Together with (3.6) these relations yield

$$H(t) = 0.53 \left(\frac{12\mu}{B}\right)^{2/15} h_\infty^{3/5} c^{4/5} t^{2/3}, \quad \hat{H}(\hat{t}) = 0.53\hat{c}^{4/5}\hat{t}^{2/3} \tag{3.8a}$$

$$L(t) = 3.54 \left(\frac{B}{12\mu}\right)^{2/15} h_\infty^{2/5} c^{1/5} t^{1/3}, \quad \hat{L}(\hat{t}) = 3.54\hat{c}^{1/5}\hat{t}^{1/3}. \tag{3.8b}$$

We note that the assumption that the healing and peeling fronts move at the same speed translates to the condition $dL/dt \ll c$, and is consistent with (3.8b) that predicts $dL/dt \to 0$ at long times while c remains constant. Figure 6 shows that the height $H(t)$ and lateral extent $L(t)$ obtained from numerical simulations are indeed close to (3.8), and figure 5(c) shows that the quartic profile (3.5) describes the blister well, validating the hypothesis of spatially invariant bending pressure within it (Flitton & King 2004; Lister *et al.* 2013).

3.4. *Peeling front mechanics*

In the region ahead of the blister, the peeling front, following the analysis of Lister *et al.* (2013) for a similar problem, we neglect van der Waals forces ahead of the blister and look

947 A16-10

for a travelling wave solution $h(x, t) = \psi(\eta)$ to (2.3). This leads to the ordinary differential equation $c\psi' + (B/12\mu)\psi^3\psi''''' = 0$. Ahead of the blister, the scale of the height is h_∞ and we therefore introduce the non-dimensionalization $\psi^\star = \psi/h_\infty = \hat{\psi}$ and $\eta^\star = \eta/L_p$, with $L_p = (Bh_\infty^3/12\mu c)^{1/5}$ a peeling length scale. This simplifies the above equation to

$$\psi^\star + \psi^{\star 3}\psi^{\star '''''} = 1 \qquad (3.9)$$

for the height profile ahead of the blister and is supplemented with the boundary conditions discussed by Lister *et al.* (2013), namely, imposing a constant curvature as $\eta^\star \to -\infty$, towards the blister, and a flat profile $\psi^\star \to 1$ as $\eta^\star \to +\infty$. In figure 5(*d*), we show the results obtained by solving the (3.9) using the bvp4c routine implemented in MATLAB and the numerical solution of the complete partial differential equation (2.5) and see good agreement between the two.

4. Consistency and robustness of different regimes/regions in elastohydrodynamic adhesion

The analysis presented in § 3 describes the whole shape of the elastic sheet. It shows different regions where the relative balances between adhesion, elasticity and fluid-driven pressure are a function of the scale separation implied by the lubrication dynamics of the squeeze flows in the narrow gap between the sheet and the substrate. We now consider the robustness of our results to variations in the details of the balances.

4.1. *Nature of the matching between the adhesion front and the blister*

The solution in the adhesion front described in § 3.2 and that of the blister described in § 3.3 need to be consistent, and so must match in the intermediate region connecting them. We find that in the adhesion front, as $\tilde{\eta} \to +\infty$ (going towards the blister), the curvature $\tilde{\kappa} \to 0$ since the height profile evolves as $\tilde{\eta}^{5/3}$. In contrast, our analysis of the solution in the blister predicts that, as $\eta \to 0$ (going towards the adhesion front), the curvature is given by (3.7), i.e. $\kappa = 1.35(12\mu c/Bh_\infty)^{2/5}$. In dimensionless units, the curvature in the blister zone is then $\tilde{\kappa} = 1.35(\sigma/h_\infty)^{1/5} = 1.35\hat{\sigma}^{1/5}$, and is therefore consistent with the curvature in the adhesion front when $1.35\hat{\sigma}^{1/5} \to 0$. This very restrictive criterion explains why the value of the prefactor in the adhesion speed in (3.3*a,b*) differs from the one observed numerically for values of $\hat{\sigma}$ that are reasonable to allow for precise numerical simulations of (2.5). Indeed, we have presented results for $\hat{\sigma} \in [0.12, 0.01]$, corresponding to $1.35\hat{\sigma}^{1/5} \in [0.88, 0.54]$, respectively. In Appendix B, we provide a brief discussion of the matching conditions connecting the adhesion front and the blister.

4.2. *Role of intermolecular potential*

While we have chosen the Lennard-Jones potential (2.1) for this study, this is but one choice of many potentials for intermolecular interactions. The physical picture we have described here is robust to alterations of the functional form of the potential, as long as it is a combination of a long-range adhesion and a short-range repulsion. None of the scaling analyses we have discussed depend on the functional form of the repulsion; only the prefactors of the quantities characterizing the adhesion front depend on it. We have verified (results not presented here) that performing simulations of (2.5) with the same attractive potential as in (2.1) but replacing the repulsive part by $\sigma^3/5h^5$ leads to the same behaviour, albeit with different prefactors for the adhesion speed, height at the tail and

maximum curvature. These prefactors can be obtained in the limit $\hat{\sigma} \to 0$ by adapting the boundary value problem (3.4) appropriately. For example, going from a repulsion potential that scales as $1/h^8$ to a weaker one evolving as $1/h^5$ decreases the adhesion speed $\tilde{C}$ from 0.281 to 0.212, decreases the maximum curvature $\tilde{\kappa}_{max}$ from 0.551 to 0.478 and increases the height at the adhesion tail $\tilde{h}_0$ from 1.017 to 1.026, but all our scaling results remain robust to this change.

4.3. *Role of far-field conditions*

The analysis of § 3.2 to characterize the adhesion front is independent of the far-field conditions and especially the height as long as $1.35\hat{\sigma}^{1/5} \ll 1$. Simulations of (2.5) with an initial condition for the height as a linear or parabolic profile, $\hat{h}(\hat{x}, \hat{t} = 0) = 0.9 + \hat{x}/10$ and $\hat{h}(\hat{x}, \hat{t} = 0) = 0.9 + \hat{x}^2/25$, respectively, indeed show a front that continues to propagate with a constant speed, with a value close to the one predicted (figure 4). However, the analysis of § 3.3 and § 3.4 for the blister shape, size and the dynamics of the peeling region needs to be adapted slightly. In particular, the relation (3.7) between the speed and curvature will be modified by the change in the far-field profile, and the assumption $dL/dt \ll c$ may not always hold anymore; we leave these studies for the future.

4.4. *Role of substrate roughness*

Our model of adhesion assumes a perfectly smooth substrate and sheet, and neglects the effects of surface roughness. At the scales involved in such instances as the adhesive bonding of silicone wafers, substrate roughness can lead to contact at asperities (Rieutord *et al.* 2006; Moriceau *et al.* 2011) or can even induce capillary condensation due to the Kelvin effect (de Boer & de Boer 2007; Fournel *et al.* 2015). These effects are challenging to model in our lubrication model, which relies on a long-wavelength analysis. Nevertheless, the scaling result (3.3*a,b*) for the adhesion speed and the profile $\tilde{f}(\tilde{\eta}) \sim \tilde{\eta}^{5/3}$ discussed in § 3.2 are consistent with experimental results (Rieutord *et al.* 2005; Navarro *et al.* 2013), with the qualification that roughness leads to a modified value of the work of adhesion $W = A/16\pi\sigma^2$.

5. Effective contact line dynamics

The question of the singular nature of the deformations of the sheet in the adhesion front is similar to but different from that seen in dewetting fluid films. To characterize this, following (3.2*a–d*), the slope of the sheet scales as $h_x \sim \sigma/l_c \sim (A/B)^{1/4} \sim \sigma^{1/2}(W/B)^{1/4}$ and the curvature scales as $h_{xx} \sim \sigma/l_c^2 \sim (A/B)^{1/2}\sigma^{-1} \sim (W/B)^{1/2}$. We see that the curvature of the sheet diverges in the contact zone as $\hat{\sigma} \to 0$, but is suppressed over a region of size $l_c \sim \sigma(B/A)^{1/4} \sim \sigma^{1/2}(B/W)^{1/4}$ determined by the balance elastic bending and the attractive part of the disjoining pressure. This scaling is consistent with the analysis of § 3.2 predicting the maximum curvature to be $\kappa_{max} = 0.551(A/6\pi B\sigma)^{1/2}$. Figure 7 shows good agreement between the numerical simulations and this prediction, and highlights the near-singular nature of the curvature.

In the limit of contact, $\hat{\sigma} = \sigma/h_\infty \to 0$ while keeping a fixed value of the work of adhesion $W = A/16\pi\sigma^2$, the slope h_x and adhesion speed c converge to zero while the curvature h_{xx} scales as $(W/B)^{1/2}$. This is in agreement with the boundary conditions for an adherent sheet, where the following applies at the stationary elastic contact line (Obreimoff 1930; Landau & Lifshitz 1986; Majidi & Adams 2009): $h(R) = 0$, $h_x(R) = 0$,
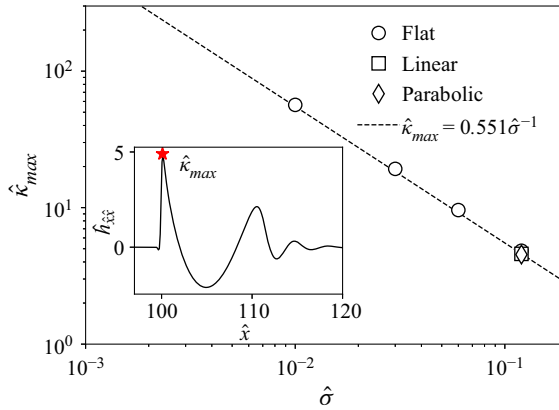
Figure 7. Characterization of the elastohydrodynamic contact zone. The maximum curvature in the contact zone, $\hat{\kappa}_{max}$, is shown for different values of $\hat{\sigma}$ and different initial profiles, illustrating the singular nature of the curvature as $\hat{\sigma} \to 0$. Results are shown by extracting the maximum curvature of the different simulations of (2.5) at $\hat{R} = 100$. The prefactor 0.551 is obtained by solving the boundary value problem (3.4) and matches well with numerical results. Inset: spatial profile of the curvature with $\hat{\sigma} = 0.12$.

$h_{xx}(R) = (2W/B)^{1/2}$. However, in the dynamic case treated in this study, this condition is replaced by a condition on the speed of the apparent contact line (3.3*a,b*). These results might be contrasted with the analogous problem of describing static and dynamic contact lines in interfacial hydrodynamics where a static contact line has a constant contact angle, whereas a dynamic contact line has a contact angle that is a function of its speed (de Gennes 1985; Bonn *et al.* 2009; Snoeijer & Andreotti 2013).

6. Conclusions

Our theoretical study of the viscously limited elastohydrodynamics of adherent sheets captures a range of different processes of dynamical adhesion, from the short-time onset of adhesion to the long-time dynamics associated with a steadily propagating adhesion front. A simple mathematical model provides a compact formulation that naturally couples the microscopic physics at the apparent elastic contact line and the macroscopic physics associated with elastic deformation and fluid flow, complementing earlier analyses of the problem. Numerical simulations reveal different regions of the sheet: an adherent zone $x < R(t)$ at constant height $h_0 \simeq \sigma$, an inner contact zone where viscous flow, elastic bending and microscale adhesion are all equally important and an outer region with $h \gg \sigma$ where the sheet is described by viscous flow and elastic bending. An asymptotic similarity analysis of the governing partial differential equation allows us to describe the full shape of the sheet and the speed of the adhesion front. In addition, we have derived the effective boundary conditions for the dynamic apparent elastic contact line, which highlights its singular nature and distinguishes it from analogous contact line conditions for a static sheet.

Just as high resolution total internal reflection fluorescence microscopy allowed for a more detailed view of the dynamics of liquid contact lines (Snoeijer & Andreotti 2013), we hope that our theoretical study might engender further experimental investigation of the nature of the elastohydrodynamic contact line that arises in a wide range of problems where elastic interfaces adhere to solid substrates in fluid environments, and for which the

actual physical mechanisms that regularize the contact line singularity in experiments can be hard to discriminate (Berhanu *et al.* 2019).

Declaration of interests. The authors report no conflict of interest.

Author ORCIDs.

- Stéphane Poulain https://orcid.org/0000-0001-8946-4968;
- Andreas Carlson https://orcid.org/0000-0002-3068-9983;
- Shreyas Mandre https://orcid.org/0000-0002-1525-8325;
- L. Mahadevan https://orcid.org/0000-0002-5114-0519.

Appendix A. Solution in the adhesion front

The fifth-order differential equation (3.4) for the function $\tilde{f}$ and the two unknowns $\tilde{C}$ and $\tilde{h}_0$ is well posed when subject to the boundary conditions discussed below, i.e. these boundary conditions correspond to seven constraints.

As $\tilde{\eta} \to -\infty$, $\tilde{f} \to \tilde{h}_0$; by letting $\tilde{f}(\tilde{\eta}) = \tilde{h}_0(1 + \tilde{g}(\tilde{\eta}))$ and substituting into (2.3) to perform a linear stability analysis of the flat state, we find that $\tilde{g}$ satisfies a linear differential equation whose solutions are linear combinations of the family of functions $\tilde{\eta} \to \exp(\omega_k \tilde{\eta})$, where the $(\omega_k)_{k=1\dots5}$ are the roots of the polynomial equation $\omega^5 + (9\tilde{h}_0^{-10} - 3\tilde{h}_0^{-4})\omega + \tilde{C}\tilde{h}_0^{-3} = 0$. We observe numerically that, for all positive $\tilde{h}_0$ and $\tilde{C}$, this equation always has exactly three solutions whose real parts are negative. The coefficients in $\tilde{g}$ associated with the latter must vanish; this shows that the asymptotic behaviour of $\tilde{f}$ as $\tilde{\eta} \to -\infty$ sets three constraints.

As $\tilde{\eta} \to +\infty$, the height of the sheet grows and we expect that $\tilde{f}(\tilde{\eta}) \gg \tilde{h}_0$ and that the contribution of the van der Waals potential becomes negligible. For large enough $\tilde{\eta}$, (3.4) then becomes approximately $\tilde{f}^3\tilde{f}''''' + \tilde{C}\tilde{f} = 0$. In the neighbourhood of the adhesion front, we expect to observe a self-similar, scale-invariant behaviour if there is a proper scale separation between the adhesion front and the rest of the sheet. The only power-law solution to $\tilde{f}^3\tilde{f}''''' + \tilde{C}\tilde{f} = 0$ is $\tilde{F}(\tilde{\eta}) = (243/280)^{1/3}\tilde{C}^{1/3}\tilde{\eta}^{5/3}$, previously discussed by Rieutord *et al.* (2005). Hence, we seek a solution to (3.4) whose asymptotic behaviour as $\tilde{\eta} \to +\infty$ is $\tilde{f}(\tilde{\eta}) \sim \tilde{F}(\tilde{\eta})$. Letting $\tilde{f}(\tilde{\eta}) = \tilde{H}(\tilde{\eta}) + \tilde{G}(\tilde{\eta})$ and neglecting second- and higher-order terms in $\tilde{G}$ gives the following differential equation: $\tilde{\eta}^5\tilde{G}''''' - (560/243)\tilde{G} = 0$. The solutions are linear combinations of the family of functions $\tilde{\eta} \to \tilde{\eta}^{\xi_k}$, where the $(\xi_k)_{k=1\dots5}$ are the five roots of the polynomial equation $(3\xi - 2)(81\xi^4 - 756\xi^3 + 2331\xi^2 - 2496\xi + 280) = 0$. Three of these solutions have a real part $\mathrm{Re}(\xi_k) > 5/3$ so that the associated coefficients must vanish. This shows that the asymptotic behaviour of $\tilde{f}$ as $\tilde{\eta} \to +\infty$ sets three constraints.

We thus see that the asymptotic behaviour of $\tilde{f}$ at $\pm\infty$ corresponds to six constraints. In addition, since we are looking for a travelling wave solution, the problem should be invariant by translation: this implies a seventh constraint and shows that solving (3.4) for $\tilde{f}$, $\tilde{C}$ and $\tilde{h}_0$ with $\tilde{f} \to \tilde{h}_0$ as $\tilde{\eta} \to -\infty$ and $\tilde{f}(\tilde{\eta}) \sim \tilde{F}(\tilde{\eta})$ as $\tilde{\eta} \to +\infty$ is a well-posed problem. We solve (3.4) numerically using the boundary value problem solver bvp4c

implemented in MATLAB, with the seven boundary conditions $\tilde{f}(-\tilde{\eta}_\infty) = \tilde{h}_0, \tilde{f}'(-\tilde{\eta}_\infty) = \tilde{f}''(-\tilde{\eta}_\infty) = 0$, and $\tilde{f}^{(n)}(\tilde{\eta}_\infty) = \tilde{F}^{(n)}(\tilde{\eta}_\infty)$ for $n = 0 \ldots 3$. We start with a small value of $\tilde{\eta}_\infty$ to facilitate convergence and iteratively increase the domain size, using solutions on smaller domains to construct an initial guess. We do so until the solution converges and does not depend significantly on the domain size. The solution is shown in figure 5(*b*), and we find that $\tilde{C} = 0.281$ and $\tilde{h}_0 = 1.017$.

Appendix B. Matching between the adhesion front and the blister

We consider here the intermediate matching region between the adhesion front (§ 3.2) and the blister (§ 3.3). The scales of this region are found by estimating when the decreasing curvature of the far-field shape of the adhesion front given by $\tilde{f}''(\tilde{\eta}) \sim (10/9)(234/280)^{1/3}\tilde{C}^{1/3}\tilde{\eta}^{-1/3}$ as $\tilde{\eta} \to \infty$ becomes comparable to the curvature of the blister, $\tilde{\kappa} = 1.35\hat{\sigma}^{1/5}$ in dimensionless units of the adhesion front. This yields the natural scales $\tilde{\eta}_0 = \tilde{C}/\tilde{\kappa}^3 \sim \hat{\sigma}^{-3/5}$ and $\tilde{f}_0 = \tilde{C}^2/\tilde{\kappa}^5 \sim \hat{\sigma}^{-1}$. Denoting by $\bar{f}$ the height and by $\bar{\eta}$ the longitudinal coordinate non-dimensionalized by these scales, and balancing the viscous and bending forces, we are led to an equation similar to that in the zippering region (§ 3.4) along with the asymptotic conditions that together read as

$$1 + \bar{f}^2\bar{f}''''' = 0, \tag{B1a}$$

$$\bar{f} \sim \left(\frac{243}{280}\right)^{1/3} \bar{\eta}^{5/3} \quad \text{as } \bar{\eta} \to 0, \quad \bar{f} \sim \frac{\bar{\eta}^2}{2} \quad \text{as } \bar{\eta} \to \infty. \tag{B1b}$$

We note that (B1*b*) sets the asymptotic behaviour of $\bar{f}$ and therefore corresponds to a sufficient number of conditions to completely determine the solution. While the reduced (B1) can be solved numerically, our results obtained from the solution of the full governing partial differential equation (2.5) for finite values of $\hat{\sigma} \in [0.01 - 0.12]$ do not reveal the structure of this intermediate region. In particular, our simulations do not exhibit a clear region with constant curvature. Therefore, we do not present results that compare these different approaches here.

REFERENCES

BALL, T.V. & NEUFELD, J.A. 2018 Static and dynamic fluid-driven fracturing of adhered elastica. *Phys. Rev. Fluids* **3** (7), 074101.

BATCHELOR, G.K. 1967 *An Introduction to Fluid Dynamics*. Cambridge University Press.

BELL, G.I. 1978 Models for the specific adhesion of cells to cells. *Science* **200** (4342), 618–627.

BELL, G.I., DEMBO, M. & BONGRAND, P. 1984 Cell adhesion, competition between nonspecific repulsion and specific bonding. *Biophys. J.* **45** (6), 1051–1064.

BENGTSSON, S., LJUNGBERG, K. & VEDDE, J. 1996 The influence of wafer dimensions on the contact wave velocity in silicon wafer bonding. *Appl. Phys. Lett.* **69** (22), 3381–3383.

BERHANU, M., GUÉRIN, A., COURRECH DU PONT, S., RAOULT, F., PERRIER, R. & MICHAUT, C. 2019 Uplift of an elastic membrane by a viscous flow. *Phys. Rev.* E **99** (4), 043102.

DE BOER, M.P. & DE BOER, P.C.T. 2007 Thermodynamics of capillary adhesion between rough surfaces. *J. Colloid Interface Sci.* **311** (1), 171–185.

BONGRAND, P. 1988 *Physical Basis of Cell-Cell adhesion*. CRC Press.

BONN, D., EGGERS, J., INDEKEU, J., MEUNIER, J. & ROLLEY, E. 2009 Wetting and spreading. *Rev. Mod. Phys.* **81** (2), 739–805.

BUTLER, M., BOX, F., ROBERT, T. & VELLA, D. 2019 Elasto-capillary adhesion: effect of deformability on adhesion strength and detachment. *Phys. Rev. Fluids* **4**, 033601.

CANTAT, I. & MISBAH, C. 1999 Dynamics and similarity laws for adhering vesicles in haptotaxis. *Phys. Rev. Lett.* **83** (1), 235–238.

CARLSON, A. 2018 Fluctuation assisted spreading of a fluid filled elastic blister. *J. Fluid Mech.* **846**, 1076–1087.

CARLSON, A., KIM, P., AMBERG, G. & STONE, H.A. 2013 Short and long time drop dynamics on lubricated substrates. *Europhys. Lett.* **104** (3), 34008.

CARLSON, A. & MAHADEVAN, L. 2016 Similarity and singularity in adhesive elastohydrodynamic touchdown. *Phys. Fluids* **28** (1), 011702.

DIRKS, J.-H. 2014 Physical principles of fluid-mediated insect attachment – shouldn't insects slip? *Beilstein J. Nanotechnol.* **5** (1), 1160–1166.

EGGERS, J. 2005 Contact line motion for partially wetting fluids. *Phys. Rev.* E **72** (6), 061605.

FLITTON, J.C. & KING, J.R. 2004 Moving-boundary and fixed-domain problems for a sixth-order thin-film equation. *Eur. J. Appl. Maths* **15** (6), 713–754.

FOURNEL, F., MARTIN-COCHER, C., RADISSON, D., LARREY, V., BECHE, E., MORALES, C., DELEAN, P.A., RIEUTORD, F. & MORICEAU, H. 2015 Water stress corrosion in bonded structures. *ECS J. Solid State Sci. Technol.* **4** (5), P124–P130.

DE GENNES, P.-G. 1985 Wetting: statics and dynamics. *Rev. Mod. Phys.* **57** (3), 827–863.

HAN, W., YU, J. & WANG, Q. 2000 Modeling the dynamics of si wafer bonding during annealing. *J. Appl. Phys.* **88** (7), 4404–4406.

HEWITT, I.J., BALMFORTH, N.J. & DE BRUYN, J.R. 2015 Elastic-plated gravity currents. *Eur. J. Appl. Maths* **26** (1), 1–31.

HOSOI, A.E. & MAHADEVAN, L. 2004 Peeling, healing, and bursting in a lubricated elastic sheet. *Phys. Rev. Lett.* **93** (13), 137802.

ISRAELACHVILI, J.N. 2011 *Intermolecular and Surface Forces*. Academic Press.

JUEL, A., PIHLER-PUZOVIĆ, D. & HEIL, M. 2018 Instabilities in blistering. *Annu. Rev. Fluid Mech.* **50**, 691–714.

KAVANAGH, J.L., ENGWELL, S.L. & MARTIN, S.A. 2018 A review of laboratory and numerical modelling in volcanology. *Solid Earth* **9** (2), 531–571.

LANDAU, L.D. & LIFSHITZ, E.M. 1986 *Course of Theoretical Physics vol. 7: Theory of Elasticity*. 3rd edn. Pergamon.

LEONG, F.Y. & CHIAM, K.-H. 2010 Adhesive dynamics of lubricated films. *Phys. Rev.* E **81** (4), 041923.

LISTER, J.R., PENG, G.G. & NEUFELD, J.A. 2013 Viscous control of peeling an elastic sheet by bending and pulling. *Phys. Rev. Lett.* **111** (15), 154501.

LISTER, J.R., SKINNER, D.J. & LARGE, T.M.J. 2019 Viscous control of shallow elastic fracture: peeling without precursors. *J. Fluid Mech.* **868**, 119–140.

LONGLEY, J.E., MAHADEVAN, L. & CHAUDHURY, M.K. 2013 How a blister heals. *Europhys. Lett.* **104** (4), 46002.

MAJIDI, C. & ADAMS, G.G. 2009 A simplified formulation of adhesion problems with elastic plates. *Proc. R. Soc.* A **465** (2107), 2217–2230.

MANI, M., GOPINATH, A. & MAHADEVAN, L. 2012 How things get stuck: kinetics, elastohydrodynamics, and soft adhesion. *Phys. Rev. Lett.* **108** (22), 226104.

MICHAUT, C. 2011 Dynamics of magmatic intrusions in the upper crust: theory and applications to laccoliths on earth and the moon. *J. Geophys. Res.* **116** (B5), B05205.

MORICEAU, H., RIEUTORD, F., FOURNEL, F., LE TIEC, Y., DI CIOCCIO, L., MORALES, C., CHARVET, A.M. & DEGUET, C. 2011 Overview of recent direct wafer bonding advances and applications. *Adv. Nat. Sci.* **1** (4), 043004.

NAVARRO, E., BRÉCHET, Y., MOREAU, R., PARDOEN, T., RASKIN, J.-P., BARTHELEMY, A. & RADU, I. 2013 Direct silicon bonding dynamics: a coupled fluid/structure analysis. *Appl. Phys. Lett.* **103** (3), 034104.

OBREIMOFF, J.W. 1930 The splitting strength of mica. *Proc. R. Soc.* A **127** (805), 290–297.

ORON, A., DAVIS, S.H. & BANKOFF, S.G. 1997 Long-scale evolution of thin liquid films. *Rev. Mod. Phys.* **69** (3), 931–980.

PEDERSEN, C., NIVEN, J.F., SALEZ, T., DALNOKI-VERESS, K. & CARLSON, A. 2019 Asymptotic regimes in elastohydrodynamic and stochastic leveling on a viscous film. *Phys. Rev. Fluids* **4**, 124003.

PENG, G.G. & LISTER, J.R. 2020 Viscous flow under an elastic sheet. *J. Fluid Mech.* **905**, A30.

PENG, G.G., PIHLER-PUZOVIC, D., JUEL, A., HEIL, M. & LISTER, J.R. 2015 Displacement flows under elastic membranes. Part 2. Analysis of interfacial effects. *J. Fluid Mech.* **784**, 512–547.

PIHLER-PUZOVIĆ, D., ILLIEN, P., HEIL, M. & JUEL, A. 2012 Suppression of complex fingerlike patterns at the interface between air and a viscous fluid by elastic membranes. *Phys. Rev. Lett.* **108** (7), 074502.

POCIUS, A.V. & DILLARD, D.A. 2002 *Adhesion Science and Engineering: Surfaces, Chemistry and Applications*. Elsevier.

RADISSON, D., FOURNEL, F. & CHARLAIX, E. 2015 Modelling of the direct bonding wave. *Microsyst. Technol.* **21** (5), 969–971.

RIEUTORD, F., BATAILLOU, B. & MORICEAU, H. 2005 Dynamics of a bonding front. *Phys. Rev. Lett.* **94** (23), 236101.

RIEUTORD, F., MORICEAU, H., BENEYTON, R., CAPELLO, L., MORALES, C. & CHARVET, A.-M. 2006 Rough surface adhesion mechanisms for wafer bonding. *ECS Trans.* **3** (6), 205–215.

RIEUTORD, F., RAUER, C. & MORICEAU, H. 2014 Interfacial closure of contacting surfaces. *Europhys. Lett.* **107** (3), 34003.

SALEM, L., GAMUS, B., OR, Y. & GAT, A.D. 2020 Leveraging viscous peeling to create and activate soft actuators and microfluidic devices. *Soft Robot.* **7** (1), 76–84.

SNOEIJER, J.H. & ANDREOTTI, B. 2013 Moving contact lines: scales, regimes, and dynamical transitions. *Annu. Rev. Fluid Mech.* **45**, 269–292.

SNOEIJER, J.H. & EGGERS, J. 2010 Asymptotic analysis of the dewetting rim. *Phys. Rev.* E **82**, 056314.

SPRINGMAN, R.M. & BASSANI, J.L. 2008 Snap transitions in adhesion. *J. Mech. Phys. Solids* **56** (6), 2358–2380.

SPRINGMAN, R.M. & BASSANI, J.L. 2009 Mechano-chemical coupling in the adhesion of thin-shell structures. *J. Mech. Phys. Solids* **57** (6), 909–931.

TONG, Q.-Y. & GÖSELE, U. 1999 *Semiconductor Wafer Bonding: Science and Technology*. John Wiley.

TURNER, K.T., THOULESS, M.D. & SPEARING, S.M. 2004 Mechanics of wafer bonding: effect of clamping. *J. Appl. Phys.* **95** (1), 349–355.

WANG, Z.-Q. & DETOURNAY, E. 2018 The tip region of a near-surface hydraulic fracture. *J. Appl. Mech.* **85** (4), 041010.

WANG, Z.-Q. & DETOURNAY, E. 2021 Force on a moving liquid blister. *J. Fluid Mech.* **918**, A15.

ZHANG, W.W. & LISTER, J.R. 1999 Similarity solutions for van der Waals rupture of a thin film on a solid substrate. *Phys. Fluids* **11** (9), 2454–2462.